ACS APPLIED MATERIALS & INTERFACES

Research Article

www.acsami.org

Crystallinity and Morphology Effects on a Solvent-Processed Solar Cell Using a Triarylamine-Substituted Squaraine

Supravat Karak,[†,‡] Paul J. Homnick,[†] Andrea M. Della Pelle,[†] Youngju Bae,[†] Volodimyr V. Duzhko,[‡] Feng Liu,[‡] Thomas P. Russell,[‡] Paul M. Lahti,*[,†] and S. Thayumanavan[†,]*

[†]Department of Chemistry and [‡]Department of Polymer Science and Engineering, University of Massachusetts, Amherst, Massachusetts 01003, United States

Supporting Information

ABSTRACT: 2,4-Bis[4′-(*N*,*N*-di(4″-hydroxyphenyl)amino)-2′,6′-dihydroxyphenyl]squaraine (Sq-TAA-OH, optical bandgap 1.4 eV, HOMO level −5.3 eV by ultraviolet photoelectron spectroscopy) is used as an active layer material in solution processed, bulk-heterojunction organic photovoltaic cells with configuration ITO/PEDOT:PSS/Sq-TAA-OH:$PC_{71}BM$/LiF/Al. Power conversion efficiencies (PCEs) up to 4.8% are obtained by a well-reproducible procedure using a mixture of good and poor Sq-TAA-OH solubilizing organic solvents, with diiodooctane (DIO) additive to make a bulk heterojunction layer, followed by thermal annealing, to give optimized V_{OC} = 0.84−0.86 V, J_{SC} = 10 mA cm^{-2}, and FF = 0.53. X-ray diffraction and scattering studies of pristine, pure Sq-TAA-OH solution-cast films show *d*-spacing features similar to single-crystal packing and spacing. The DIO additive in a good solvent/poor solvent mixture apparently broadens the size distribution of Sq-TAA-OH crystallites in pristine films, but thermal annealing provides a narrower size distribution. Direct X-ray diffraction and scattering morphological studies of "as-fabricated" active layers show improved Sq-TAA-OH/$PC_{71}BM$ phase separation and formation of crystallites, ∼48 nm in size, under conditions that give the best PCE.

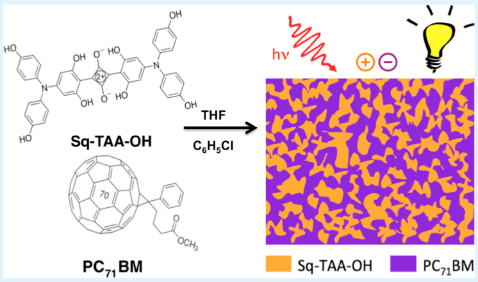

KEYWORDS: *solution-processed photovoltaic devices, molecule-based solar cells, squaraines, triarylamines, N,N-diarylanilinosquaraines, organic bulk heterojunctions*

INTRODUCTION

By comparison to inorganic substances, organic semiconductors have several key advantages for use in electronic devices, including solution processability, light weight, structural and electronic tunability, and mechanical flexibility. These characteristics make them highly promising as low cost electronic materials for large-scale technologies in next-generation devices. Organic materials have attracted great scientific interest for possible use in field effect transistors (FETs),[1] organic light-emitting diodes (OLEDs)[2,3] and, most recently, organic photovoltaic (OPV) devices. OPVs show promise for major impact in solar energy technologies, if they can be made cost-effectively with sufficiently good power conversion efficiency (PCE, η) in larger devices.[4−8] Also organic semiconductors are environmentally promising materials whose development would reduce anthropogenic greenhouse gas emission, and toxicity concerns by comparison to inorganic semiconductors like cadmium, tellurium, and arsenic.[9] At present, OPV device efficiencies have reached PCE of ∼10% for single bulk heterojunction and multijunction solar cells, despite challenges of short exciton diffusion lengths[10] and limits on active layer solar panchromism. Donor/acceptor (D/A) bulk heterojunction (BHJ) fabrication techniques that produce large, bicontinuous D/A interphase contact areas are now being widely used as a strategy for maximizing OPV PCE.[4,5,8] To achieve optimal BHJ morphologies, different approaches have been used to fabricate the active layer, including thermal and solvent annealing,[11,12] controlled solvent evaporation,[13,14] and use of low volatility solvent additives.[15−18] However, such random interpenetrating D/A networks can still lead to poor charge carrier transport with charge trapping, because of nonuniform scales of D/A phase separation and formation of structural charge-trapping sites,[19,20] especially in thicker films. To improve OPV BHJ solar cell performance, development of new photoactive materials with stronger and broader absorption remains an area of intense work. Equally important is the ease of processability for any new materials, to enable morphological optimization with corresponding improvement of charge mobility and PCE.

Squaraine dye derivatives (SQ, Scheme 1) are very promising OPV active layer electronic materials.[21,22] In addition to vapor deposition of SQ derivatives,[23,24] much effort is being put into optimizing various SQ-based BHJ-type OPV devices through tuning and optimizing active layer morphology primarily by solution processing. Although BHJ cells can be challenging to optimize, they provide multiple variables for improving PCE by using up-scalable solution processing fabrication procedures that are appropriate for large area industrial development. In

Received: March 31, 2014
Accepted: July 1, 2014
Published: July 14, 2014

Scheme 1. Squaraine Derivatives of Interest for Organic Photovoltaics

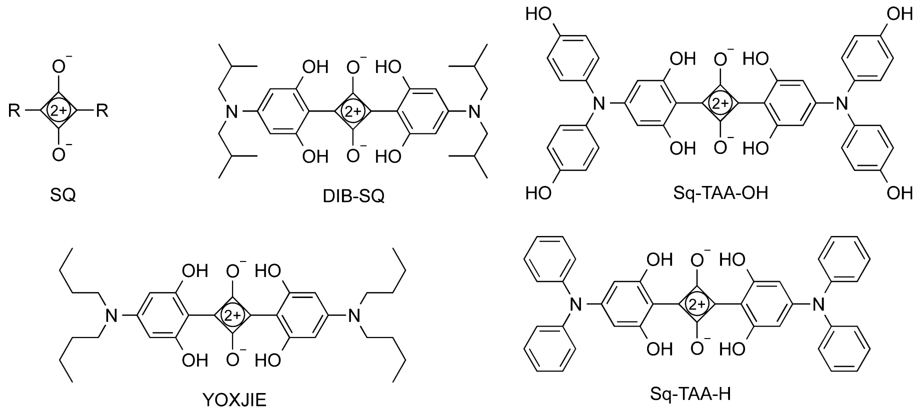

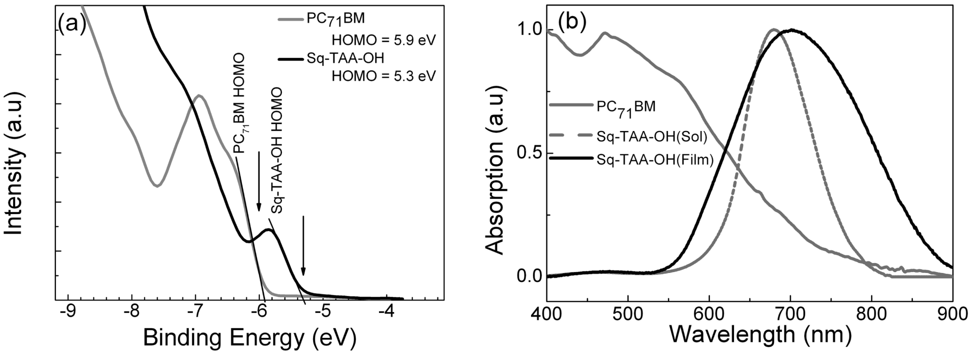

Figure 1. (a) UPS spectra of Sq-TAA-OH (black line) and $PC_{71}BM$ (gray line) on ITO/PEDOT:PSS substrates around the energy region near the HOMO levels; (b) normalized UV−visible absorption spectra of Sq-TAA-OH (gray dashes = THF solution, black line = film) and $PC_{71}BM$ (gray line = film).

2008, Marks and co-workers reported a 1.24% PCE using 2,4-bis[{5-diphenylhydrazonyl}-1-alkylpyrrol-2-yl]squaraines by a BHJ solution processing procedure.[25] Forrest, Thompson and co-workers have improved the PCE of OPV devices with SQ derivatives through numerous studies, using both vapor deposited and solution processed device active layers.[26−29] By 2012, Yang and co-workers[30] reported PCE = 6.3% for single-junction, solution-fabricated solar cells with an active layer of 2,4-bis[4′-*N*,*N*-di(isobutyl)amino)-2′,6′-dihydroxyphenyl]-squaraine (DIB-SQ, Scheme 1) and $PC_{71}BM$.

Further optimization of solar cells based on SQ derivatives requires electronic tuning at both individual molecule and supramolecular levels. Molecular level electronic tuning can be achieved by structural variation, but must be followed by supramolecular electronic tuning of solid film light absorption characteristics and photogenerated charge transport properties that arise from both nanoscopic and mesoscopic scale molecular solid state assembly. In this report, a new substituted triarylamine SQ derivative, 2,4-bis[4′-(*N*,*N*-di(4″-hydroxyphenyl)amino)-2′,6′-dihydroxyphenyl]squaraine (Sq-TAA-OH) is used as a substituent-tuned hole-transport component of BHJ solution-processed OPVs. The morphology of BHJ active layer films of Sq-TAA-OH with $PC_{71}BM$ electron transporting material was adjusted by varying device-processing conditions to optimize PCE to nearly 5%. Use of good/bad solvent mixtures, low volatility processing additives, and postfabrication thermal treatment all play important roles to optimize the PCE. Most importantly, studies of the as-fabricated device morphologies by a combination of X-ray diffraction and scattering techniques provide a clear correlation of PCE increases with crystallinity and size scale of phase separation in the bulk heterojunction. The results of the study demonstrate how linking PCE performance improvements to specific morphological size-scale features is important to advance the promise[30] of SQ-based BHJ OPVs made by straightforward solvent-based procedures.

■ RESULTS AND DISCUSSION

The BHJ devices in this study were fabricated using Sq-TAA-OH (Scheme 1) as the active layer donor (D) material and $PC_{71}BM$ as the acceptor (A) material. Sq-TAA-OH was selected for testing from a set of recently described SQ analogues[31] whose energy levels were tuned by substituent variation. To establish HOMO levels for Sq-TAA-OH and $PC_{71}BM$ under device-relevant conditions, UPS measurements were performed on solid state films (Figure 1). These yielded energy levels of −5.3 and −5.9 eV, respectively. Sq-TAA-OH thus has a relatively low optical bandgap and a HOMO energy that should provide a relatively high V_{OC} based on literature[32] analogies. UV−vis absorption spectra of solutions and solid films were also measured, as shown in Figure 1b. In the good solvent THF, Sq-TAA-OH has a strong molar absorptivity of 91,400 M^{-1} cm^{-1} at λ_{max} = 680 nm, with an absorption onset (λ_{onset}) at 780 nm or 1.6 eV. By comparison, the neat Sq-TAA-OH solid film absorption is red-shifted to λ_{max} ~700 nm, with λ_{onset} ~890 nm or 1.4 eV. A solid film of $PC_{71}BM$ showed a gradual λ_{onset} ~730 nm or 1.7 eV. The UV−vis onset energies of the solid films were then used as bandgap energy estimates and combined with the respective UPS HOMO energies to give LUMO energies of −3.9 and −4.2 eV for Sq-TAA-OH and

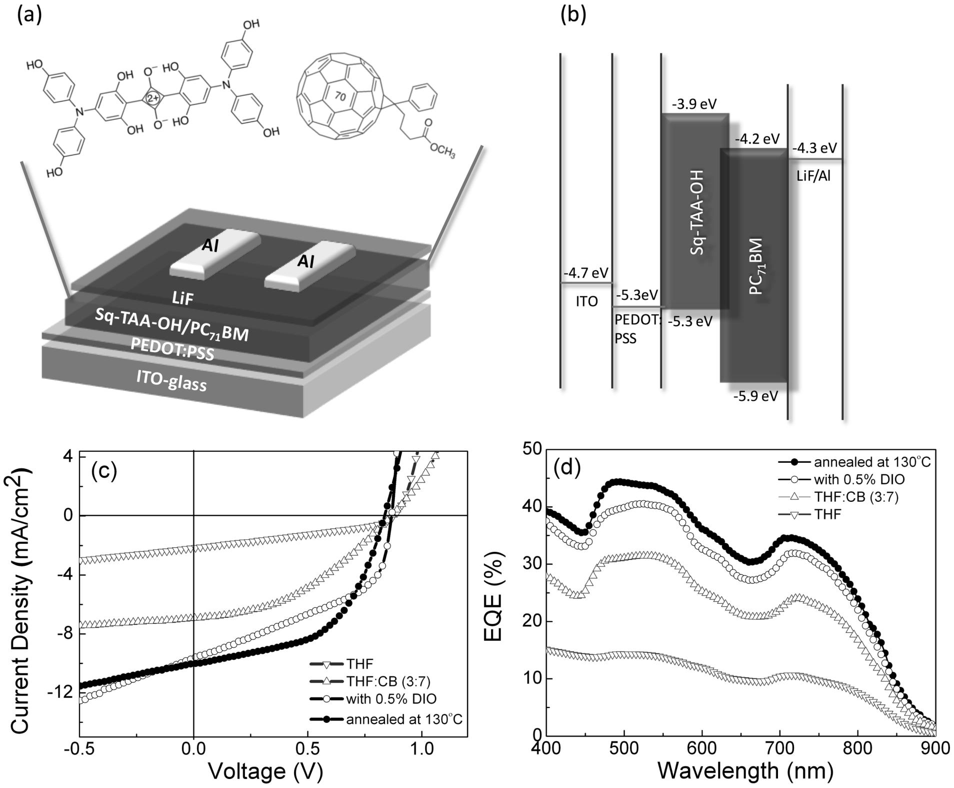

Figure 2. (a) Schematic diagram of device configuration of Sq-TAA-OH and PC$_{71}$BM. (b) Energy level diagram of ITO/PEDOT:PSS/Sq-TAA-OH:PC$_{71}$BM/LiF/Al solar cell. (c) Current density−voltage characteristics of the devices for different processing conditions under 100 mW/cm^2 AM 1.5 simulated solar irradiation and (d) external quantum efficiency (EQE) spectra of the corresponding devices from (c).

PC$_{71}$BM, respectively. For these energies, the Sq-TAA-OH to PC$_{71}$BM LUMO offset is ∼0.3 eV, sufficient to favor exciton dissociation at the donor/acceptor interfaces. In earlier work, some of us reported[31] a thin-film, reduction potential based estimate of −4.18 eV for the Sq-TAA-OH LUMO energy, which would suggest less driving force for exciton dissociation at Sq-TAA-OH:PC$_{71}$BM interfaces. Still, the promising PCEs reported below for optimized Sq-TAA-OH:PC$_{71}$BM devices seem more consistent with effective downhill energetics for exciton dissociation. Finally, the Sq-TAA-OH HOMO to PC$_{71}$BM LUMO offset of ∼1.1 eV suggests that relatively high V_{OC} can be achieved: this expectation was realized, as described below.

The best ratio of Sq-TAA-OH:PC$_{71}$BM for maximizing PCE was determined by varying their weight/weight (w/w) ratio in devices having a ITO/PEDOT:PSS/Sq-TAA-OH:PC$_{71}$BM/LiF/Al configuration (Figure 2), using active layer films that were spin-coated from THF, which is a good solvent for both organic components. The device performance characteristics for the active layer component ratio optimization experiments are given in the Supporting Information (Figure S1, Table S1). Performance results using the optimized 1:5 (w/w) Sq-TAA-OH:PC$_{71}$BM ratio are shown in Figure 2. This 1:5 Sq-TAA-OH:PC$_{71}$BM ratio was maintained for all device optimization experiments described below. Yang and co-workers,[30] similarly, found maximum PCE performance with 1:4 to 1:6 (w/w) ratios of DIB-SQ/PC$_{71}$BM in solution-processed BHJ devices.

Figure 3 compares UV−vis absorption spectra for films of the 1:5 w/w Sq-TAA-OH:PC$_{71}$BM blend ratio that were spin-coated using different solvent ratios of THF and chlorobenzene (CB). THF is a good solvent for dissolving Sq-TAA-OH, with a low boiling temperature of 66 °C, while CB is a bad solvent for dissolving Sq-TAA-OH with a high boiling temperature of 131 °C. In all of the mixture films, Sq-TAA-OH contributes strong absorption over 550−880 nm with a peak at 700−725 nm, whereas PC$_{71}$BM contributes absorption over 400−650 nm. Overall, the mixed films show very good panchromic visible spectrum absorption, with some variation depending on solvent casting conditions.

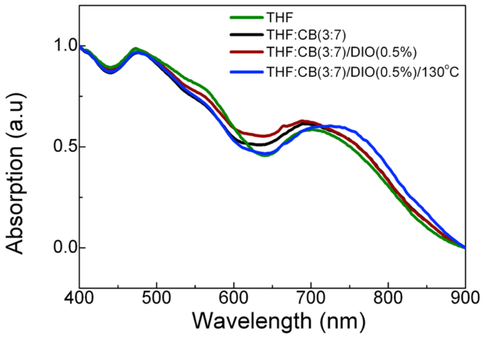

Figure 3. Normalized UV−visible absorption spectra of the BHJ films of 1:5 (w/w) Sq-TAA-OH:PC$_{71}$BM processed under different conditions.

Sq-TAA-OH:PC$_{71}$BM films spin-coated from THF show λ_{onset} ∼888 nm, similar to the onset for neat Sq-TAA-OH films (see the Supporting Material, Figure S2). By comparison, films coated from a 30:70 volume/volume (v/v) THF:CB solution show a small blue shift in λ_{max}, but a small red-shift in λ_{onset} to ∼900 nm. Addition of 0.5% (volume) of high boiling 1,8-diiodooctane (DIO) to the THF:CB film-casting solvent mixture scarcely changed either the absorption maximum or onset, but did increase the optical density in the 600−700 nm region where there is a spectral minimum for Sq-TAA-OH:$PC_{71}BM$ films.

During casting of Sq-TAA-OH:$PC_{71}BM$ mixtures from solvent blends, the lower boiling, good solvent THF evaporates first, decreasing the solubility of the Sq-TAA-OH, while keeping $PC_{71}BM$ fully solubilized in CB and DIO. In principle, Sq-TAA-OH can then crystallize into ordered phase domains, while the remaining $PC_{71}BM$ is forced into vacant interspatial regions to give the desired BHJ-type phase separation. As an additional step to tune the active layer thin film morphology, devices processed from 30:70 THF:CB mixture with 0.5% DIO were also thermally conditioned at 130 °C for 10 min. These annealed films exhibited an absorption spectrum having a broadened 700−800 nm region with λ_{max} ~725 nm and a red-shifted λ_{onset} ~912 nm. As will be shown by experimental evidence described below, the thermal conditioning step that gives the improved PCE also increases Sq-TAA-OH crystallinity and phase separation, factors that are expected to improve charge transport.

Figure 2 includes the current density vs voltage (J−V) characteristics under AM 1.5 simulated solar irradiation conditions at 100 mW cm^{-2} for the devices made using Figure 3 processing conditions, versus the initial THF-only fabrication results. Key device performance parameters are summarized in Table 1. The initial device spin-coated from THF without cosolvents or thermal conditioning gave an open-circuit voltage V_{OC} = 0.86 V, with a short-circuit current density J_{SC} = 2.15 mA cm^{-2} and a fill factor (FF) of 33.6%: the overall PCE was η = 0.63%. Devices fabricated from mixed solvent gave maximized η = 2.44% for 30:70 v/v THF:CB, with V_{OC} = 0.87 V and improvement of both J_{SC} and FF: performance parameters are given in Supporting Information for devices made using other solvent ratios. Devices fabricated at ambient temperature with 30:70 v/v THF:CB plus 0.5 v% DIO further improved PCE to η = 3.74%, with V_{OC} remaining at 0.87 V but improved J_{SC} of 9.58 mA cm^{-2} and FF of 44.8%. But, the latter devices thermally conditioned at 130 °C for 10 min gave an average η = 4.44% (maximum η = 4.8%), again with V_{OC} remaining steady at 0.84 V, and with J_{SC} increased to 10.01 mA cm^{-2} at FF = 52.8%.

Table 1. Device Performance for SQ-OH:$PC_{71}BM$-Based Solar Cells Fabricated Using Different Processing Conditions

sample	J_{SC} (mA/cm^2)	V_{OC} (V)	FF (%)	PCE, η (%)
THF	2.15	0.86	33.6	0.63
THF:CB (3:7)	6.92	0.87	40.5	2.44
THF:CB (3:7) with DIO (0.5%)	9.58	0.87	44.8	3.74
THF:CB (3:7) with DIO (0.5%), anneal at 130 °C for 10 min	10.01	0.84	52.8	4.44

The improved cell performance with different solvent and annealing procedures is due to increased J_{SC} and FF. The steady V_{OC} under the various conditions tested indicates that there is no significant variation in the D−A HOMO−LUMO level energetics shown in Figure 2(b). The significantly lower FF in devices spin-coated from THF is attributable to poor BHJ morphology, and is consistent with excessive charge-pair recombination. The optimized J_{SC} from mixed solvent fabrication is 5-fold higher than that in THF-only processed devices, even without thermal conditioning. This suggests formation of a good BHJ Sq-TAA-OH:$PC_{71}BM$ blend morphology with much increased D/A interface area to improve probability of exciton dissociation, with more continuous conducting paths for free charge movement.

External quantum efficiency (EQE) spectra were compared for the differently processed devices, as shown in Figure 2d. The spectra closely correspond to the Sq-TAA-OH:$PC_{71}BM$ film UV−vis absorption profiles. The maximum EQE of ~15% in the THF-only processed devices increases to ~32% in the mixed solvent based devices, and reaches a maximum of ~45% for the optimized device processed with the mixed solvent system plus DIO with thermal conditioning. Figure 2d also shows that the devices with optimized processing conditions showed higher spectral response in both the Sq-TAA-OH (550−880 nm) and $PC_{71}BM$ (400−650 nm) absorption regions, by comparison to the fairly diffuse response trace of THF-only processed devices. This is consistent with the solvent induced morphology optimization giving improved exciton dissociation efficiency in both donor and acceptor phases, which would be expected for BHJ phase separation.

The effects of Sq-TAA-OH:$PC_{71}BM$ film fabrication conditions on the intrinsic diode properties of these devices were also probed by investigating their dark current characteristics (Figure 4). The devices exhibit typical rectifying diode behavior, with quite different J−V curves under forward and reverse bias conditions for the different processing conditions. This indicates a significant variation of energy barriers for charge flow at active component interfaces. The devices

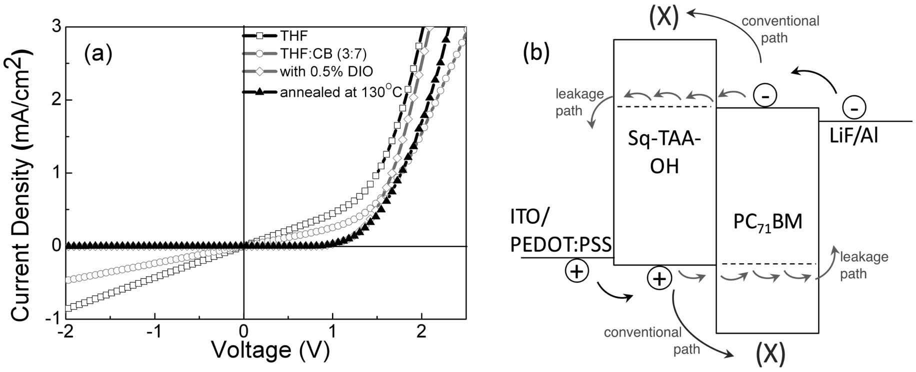

Figure 4. (a) Dark current density−voltage plots of devices made using different processing conditions. (b) Schematic model of charge transport from electrodes through Sq-TAA-OH donor and $PC_{71}BM$ acceptor for unoptimized morphology with a leaky interface: Arrows show the leakage path with reduced barrier height and the conventional path for charges.

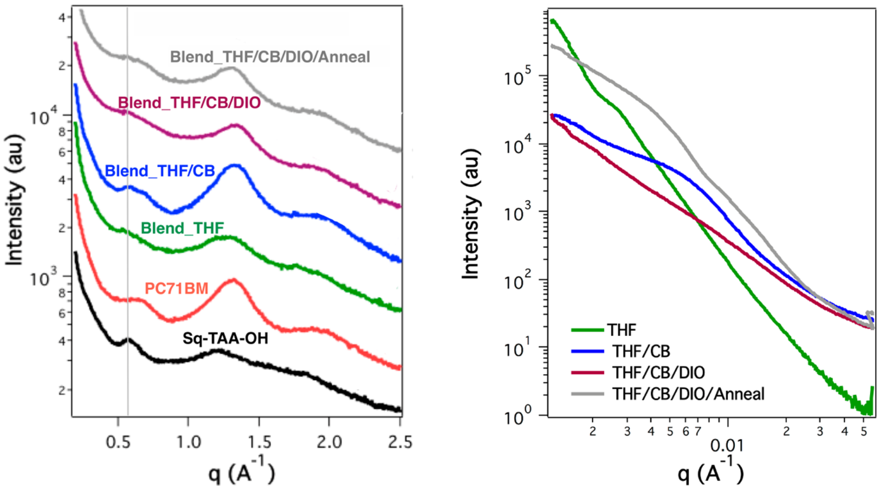

Figure 5. GIXD (left) comparing results for films of pure Sq-TAA-OH and $PC_{71}BM$ to 1:5 (w/w) Sq-TAA-OH:$PC_{71}BM$ blends fabricated under different processing conditions. RSoXS (right) compares results for 1:5 (w/w) Sq-TAA-OH:$PC_{71}BM$ blend films.

processed from pure THF and from the THF:CB mixed solvent without DIO additive showed relatively higher leakage current with a rectification ratio of ~10 (at ± 3 V): the devices processed with mixed solvent and DIO exhibited a much higher rectification ratio of $\sim 1 \times 10^3$, with and without annealing.

Although the FF of our devices after thermal annealing is quite competitive among purely solution-processed squaraine devices, it is rather lower than FF in some squaraine incorporating devices processed (at least in part) by thermal evaporation. This is attributable to relatively low shunt resistance (R_{SH}) with high series resistance (R_S) in the Sq-TAA-OH:$PC_{71}BM$ devices. Ideally[33] shunt resistance should be high ($R_{SH} \approx 1 \times 10^3$ to 1×10^4 Ω cm^2) and series resistance should be low ($R_S \approx 0.1-10$ Ω cm^2) to achieve the best FF. But, the best PCE devices in the present study gave relatively low $R_{SH} \approx 3.49 \times 10^2$ Ω cm^2 and high $R_S \approx 17.54$ Ω cm^2. These results possibly originate from nonuniform phase separation in the bulk heterojunction between Sq-TAA-OH and $PC_{71}BM$ during film casting. This could create pinholes and defect leakage paths that are much reduced, but not fully eliminated, by use of solvent additive DIO and subsequent thermal annealing. X-ray diffraction studies described below support a nonuniform phase separation in as-fabricated Sq-TAA-OH:$PC_{71}BM$ films.

Figure 4b shows a putative model of charge transport based on Figure 2b energy scheme, which addresses the observed changes in device diode properties with changing fabrication conditions. If a sharp interface with vertical phase separation forms between Sq-TAA-OH and $PC_{71}BM$ during film casting, holes and electrons can be easily injected from ITO and Al electrodes under forward bias, but will face a significant barrier at Sq-TAA-OH/$PC_{71}BM$ interfaces. Therefore, the current onset is mainly determined by injection of charges at the Sq-TAA-OH/$PC_{71}BM$ interface. Under reverse bias, holes can scarcely be injected at Al/$PC_{71}BM$ cathode junctions, and electrons face a high barrier at ITO/Sq-TAA-OH junctions, yielding strongly rectified behavior of a good diode device. Presumably, during film casting from single solvent THF or even the THF:CB mixed solvent without the DIO additive, neither a sharp interface nor a strongly vertical phase separation occurs between Sq-TAA-OH and $PC_{71}BM$. The phases are intermingled substantially throughout the device active layer, reducing the effective barrier height for charge transport and increasing leakage current. With use of the DIO additive and thermal annealing, morphological separation becomes sharper and leakage current decreases considerably. These changes do not completely offset shunt/series resistance mismatches discussed in the previous paragraph, but they substantially improve device PCE, presumably in part by healing pinholes and leakage defects.

The nature of the morphology changes inferred from changes in spectral or electrical behavior was confirmed by direct studies of the Sq-TAA-OH thin films and blended films with $PC_{71}BM$, using grazing incidence X-ray diffraction (GIXD). Figure 5 shows out-of-plane line-cut profiles for results obtained with films prepared under "as fabricated" device conditions, and Figure S4 in the Supporting Information shows the actual diffraction patterns. The neat $PC_{71}BM$ thin film showed three typical[34] diffractions at 0.68 Å^{-1}, 1.32 Å^{-1} and 1.95 Å^{-1}. The neat Sq-TAA-OH thin film showed a peak at 0.6 Å^{-1} in the out-of-plane direction (Figure 5a), corresponding to ~1 nm *d*-spacing.

Forrest, Thompson, and co-workers have put considerable and detailed efforts into correlating performance metrics for SQ-based organic solar cells with *d*-spacings from electron diffraction patterns obtained from thin films deposited on substrates under conditions similar to those used for fabricating devices.[26−28,35,36] The relationship seems complex, especially given the effect of film roughness on PCE, and on how thermal or solvent vapor annealing influences formation of crystallites. In the present case, the *d*-spacings observed in the pure spin-cast films of Sq-TAA-OH can be compared to crystallographic packing that was obtained from single crystal X-ray diffraction analysis. Details of the single crystal analysis are given in the Supporting Information in Tables S2 and S3 and in a separate CIF format file (ORTEP representation in Figure S5 in the Supporting Information). There are relatively few crystallographic reports for SQ derivatives (Cambridge Structure Database, version 5.35). Dirk et al. reported that YOXJIE (Scheme 1)[37] forms stacks with a slip stack angle of 47.0° along the molecular long axis, at a plane-to-plane stack distance of 3.38 Å between four-member rings. Thompson, Forrest and co-workers have reported[32] crystal structures for DIB-SQ and Sq-TAA-H (Scheme 1), and found that the latter forms slip-stacks similar to those in YOXJIE and (as described below) in Sq-TAA-OH.

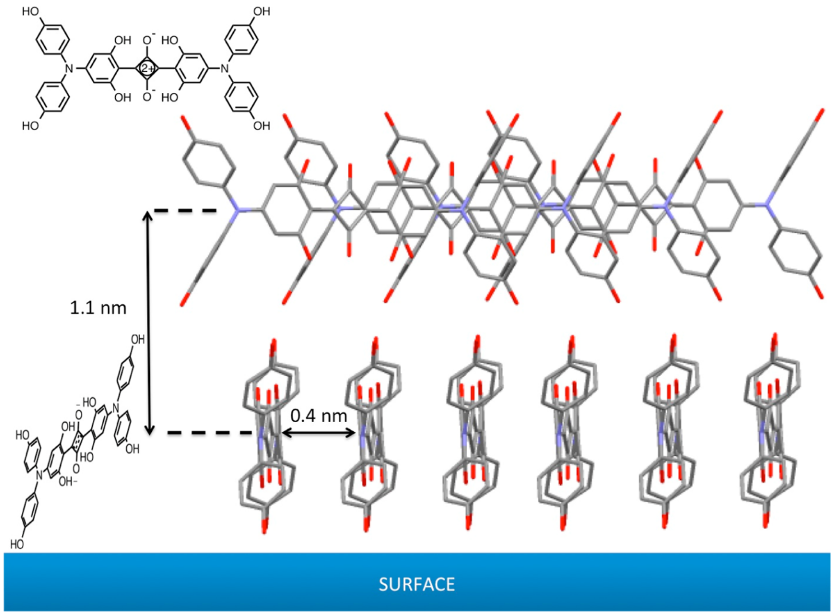

Figure 6. Sq-TAA-OH crystallographic packing spacing from single crystal diffraction results, with proposed orientation for stacking in a thin film.

From multiple solvent systems, Sq-TAA-OH formed crystals that decomposed upon standing under ambient open-air room conditions, but it did form a stable cocrystal from acetone layered below hexane. Strong intramolecular hydrogen bonds enforce planarity in the tetrahydroxydiphenyl-squaric acid framework. This assists stacking of Sq-TAA-OH, but with a 69.2° slip stack angle and a stacking distance of 4.1 Å from one dihydroxyphenyl ring to the one closely stacked above it. The stacks of Sq-TAA-OH molecules form slabs well-separated by columns of acetone solvate molecules.

Although the single-crystal packing of Sq-TAA-OH need not necessarily reflect molecular packing that might occur in a spin-coated film, the spacing between the slabs of π-stacked Sq-TAA-OH molecules corresponds closely to the out-of-plane 0.6 $Å^{-1}$ feature in the GIXD shown in Figure 5(a). The diffraction image also shows a complementary arc for the in-plane region at 1.53 $Å^{-1}$ (see Figure S4 in the Supporting Information), corresponding to a 0.41 nm spacing. This is a spacing usually assigned to (010) $\pi-\pi$ stacking in conjugated polymers and elongated, conjugated organic molecules:[38,39] it corresponds well to the slip stacked π stacking distance in the Sq-TAA-OH·(acetone) cocrystal. Combining the GIXD out-of-plane and in-plane spacings to spacings in the Sq-TAA-OH·(acetone) cocrystal suggests that the Sq-TAA-OH molecules have an edge-on π stacking orientation as pure thin films. Figure 6 shows this proposed stacking scheme, with crystallographic distances that correspond to the *d*-spacings described above. Stacking edge-on to the surface seems unlikely to enable good charge transport perpendicular to the surface (the geometry appropriate for an OPV device). Of course, the pure film Sq-TAA-OH would not necessarily give the same Sq-TAA-OH assemblies as the Sq-TAA-OH:PC$_{71}$BM mixture films. Still, comparisons of the GIXD profiles in Figure 5a to one another and to resonant soft X-ray scattering (RSoXS) results in Figure 5b provide important insights to correlate morphological size scale with PCE in this study.

There is much less Sq-TAA-OH than PC$_{71}$BM in the mixed composition BHJ films, so Sq-TAA-OH is harder to observe in GIXD under those conditions. The GIXD out-of-plane traces for the BHJ films all appear roughly to arise from simple addition of the pure component diffraction traces. The films from the good solvent THF give broadened and weak peaks that indicate intermingling of phases. Although atomic force microscopy examination is uninformative for these smooth and essentially featureless films, GIXD shows the THF/CB solvent mixtures to give enhanced diffraction features assignable to both Sq-TAA-OH and PC$_{71}$BM, indicating improved crystallization and separation of the individual component phases. The improved phase separation correlates with the strong increase in PCE using the THF/CB solvent processing (Table 1). Notably, using just 0.5 volume-% of DIO additive in processing significantly reduces Sq-TAA-OH ordering for films cast at ambient temperature, as seen from the broadening and reduced intensity of the peaks, although PCE still increases.

A significant additional increase in PCE that occurs upon 130 °C thermal conditioning of the THF:CB:(0.5% DIO) fabricated BHJ device with DIO (0.5%) was not accompanied by any obvious change in the GIXD trace relative to the unannealed trace (Figure 5a). This indicated a post-annealing morphological change, at a size scale that is not probed by GIXD. Therefore, the lateral morphology of the blends was probed by resonant soft X-ray scattering (RSoXS) at the carbon K-edge, a method frequently used to probe the size scale of phase separation in polymer blends or related OPV active layers.[40,41] The results are shown in Figure 5b. Sq-TAA-OH:PC$_{71}$BM blend films processed from THF alone showed a rapid decay in intensity with increasing *q*. This is similar to the behavior seen for large scale phase separation in polymer:PCBM blends,[42] with PC$_{71}$BM aggregation. The inter-domain spacing was beyond the resolution limit. This would cause significantly reduced interfacial area in the D/A interfaces, and explain the low J_{sc} from the THF-only devices (2.15 mA/cm, Table 1). By comparison, THF:CB solvent mixture processing gave a diffraction shoulder at ~0.0066 $Å^{-1}$, corresponding to formation of features with a spacing of 92 nm. This is moderate by comparison to spacing in other organic photovoltaic BHJ phases,[38] and is consistent with the improved J_{SC} and PCE of THF:CB fabricated devices relative to THF-only processed devices. Because the blend ratio uses excess PC$_{71}$BM, the observed phase separation spacing more than likely arises from Sq-TAA-OH intercrystal spacing in a background of PC$_{71}$BM: in a well-mixed phase, only crystals will readily be seen, and PCBM crystals are difficult to observe.

Interestingly, THF/CB/(0.5% DIO) processed thin films did not show *any* well-pronounced feature size in RSoXS, suggesting that added DIO gave a relatively broad distribution of Sq-TAA-OH in a PCBM-rich background. Because devices fabricated using these conditions still showed improvement compared to THF/CB processing without DIO (Table 1), the nearly featureless scattering intensity profile may arise from an ensemble of features over a wide range of sizes. Figure 7 schematically represents the putative differences between the Sq-TAA-OH:PC$_{71}$BM heterojunction percolation networks processed with and without DIO, especially the smaller typical size of Sq-TAA-OH domains with DIO that form with a fairly wide range of domain sizes. But, thermal annealing of the THF/CB/(0.5% DIO) processed thin films for the same duration used for carry out PCE testing of OPV devices produced RSoXS scattering features at 0.0041 Å^{-1} (153 nm spacing) and 0.013 Å^{-1} (48 nm spacing). This clearly shows that the annealing step recovers a narrower, more readily identified distribution of RSoXS-detectable crystallite sizes than is formed with DIO additive *sans* annealing. The smaller size-scale RSoXS scattering features that appear only in the additive-plus-annealing sequence seem likely to be responsible for the higher mobility of photogenerated charges and current flow observed under processing conditions that gave the best device PCE performance observed in this study.

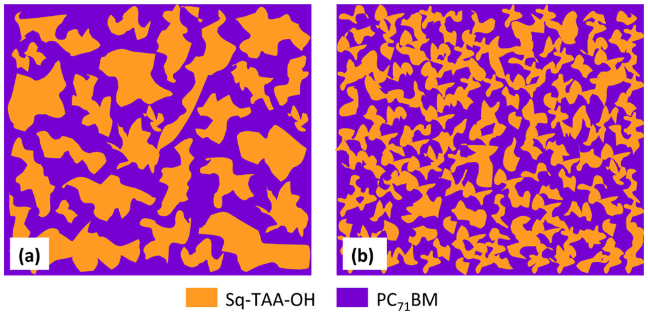

Figure 7. Schematic diagram of the active layer percolation network for Sq-TAA-OH:PC$_{71}$BM thin film processed (a) without additives and (b) with additives.

CONCLUSIONS

Sq-TAA-OH is a promising variant of the squaraine family of low-bandgap, high-absorptivity hole-transporting molecules for OPVs. Solution-processed OPV BHJ type cells with Sq-TAA-OH gave very good photoconversion device performance that was strongly and reproducibly dependent on active layer morphology modification. Optimization of good-bad mixed solvent ratio, use of DIO as a solvent additive, and postfabrication thermal film annealing all play important roles in enhancing the device efficiency through increasing short-circuit current and fill factor. A maximum device PCE of η = 4.80% is realized, with multiple devices under optimized conditions giving average η = 4.44% with V_{OC} = 0.84 V, J_{SC} = 10 mA cm^{-2}, and FF = 0.53. The optimized PCE is 7-fold higher than is found in devices processed from good solvent THF alone without thermal conditioning or solvent additives. The improvement is attributed to the formation of active layer morphology with better π-system stacking of Sq-TAA-OH and improved PC$_{71}$BM phase crystallinity. The improved photovoltaic performance metrics correlate with "as fabricated" X-ray diffraction and scattering studies showing a likely nanoscale Sq-TAA-OH π-system stacking from single crystal studies, and a likely 48 nm size scale morphology for phase separation of Sq-TAA-OH crystallites. The study demonstrates the value of simultaneously testing photovoltaic performance and active layer morphology for rational device optimization, and opens new prospects for developing high-efficiency solution processable OPV devices using functionalized bis(triarylamino)-squaraine derivatives as active layer materials.

EXPERIMENTAL SECTION

Materials. [6,6]-Phenyl-C$_{71}$-butyric acid methyl ester (PC$_{71}$BM) was obtained from American Dye Source and used as received. 1,8-Diiodooctane (DIO, 98%), tetrahydrofuran (THF, 99.5%), and chlorobenzene (CB, 99.8%) were purchased from Sigma-Aldrich and used without further purification.

Sq-TAA-OH was synthesized and purified as described in the literature.[25] Green powder, mp >260 °C; ^{1}H NMR (400 MHz, DMSO-d_6, δ): 11.3 (s, 4H, internal OH), 9.76 (s, 4H, OH), 7.14 (d, J = 8 Hz, 8H; Ar H), 6.82 (d, J = 8 Hz, 8H; Ar H), 5.47 (s, 4H; internal Ar H); ^{13}C NMR (100 MHz, DMSO-d_6, δ): 180.59 (C═O), 164.39, 162.21, 159.24, 156.61, 135.08, 128.74, 116.36, 103.25, 95.79; ATR-IR: ν = 3500−2500 (v br, OH), 3050 (w, aryl C−H), 1623 (m, C═O), 1208 (vs, C−O); UV−vis (tetrahydrofuran): λ_{max} (ε) = 680 nm (91,400 M^{-1}cm^{-1}); MS (FAB) m/z: calcd for $C_{40}H_{28}N_2O_{10}$, 696.18 [M$^+$]; found, 696.18.

Device Preparation. The photovoltaic device architecture used was ITO/PEDOT:PSS (40 nm)/Sq-TAA-OH:PC$_{71}$BM (70 nm)/LiF (1.5 nm)/Al (100 nm). ITO substrates (20 Ω/sq, from Thin Film Devices) were cleaned using Mucasol detergent (Aldrich, pH 13), deionized water, acetone, and then isopropyl alcohol sequentially with 10 min of ultrasonication in each step. The cleaned ITO surface was exposed to UV/ozone treatment for 20 min, then a PEDOT:PSS solution (Heraeus Clevios P VP AI 4083) was spin-coated for 2 min at 2000 rpm to form a hole transport layer, which was then thermally conditioned at 150 °C for 30 min in air to give a PEDOT:PSS film thickness of ~40 nm as measured by profilometry.

Based on experiments testing various relative amounts of Sq-TAA-OH:PC$_{71}$BM, a 1:5 weight ratio blend solution of total 30 mg/mL was prepared using different solvents as described subsequently. After stirring overnight at 55 °C inside a glovebox (nitrogen, <1 ppm of O_2, <1 ppm of H_2O) the solution was heated to 90 °C for 15 min, then quickly spin-casting while still hot at 1500 rpm for 60 s onto the ITO/PEDOT:PSS substrate. The coated films were heated at 80 °C for 10 min to evaporate residual solvent. A 1.5 nm LiF buffer layer was vapor-deposited at 1×10^{-6} Torr, followed by a 100 nm thick Al cathode layer at the same vacuum conditions. The mask that was used gave an effective device area of 0.06 cm^2.

Electronic Properties of Materials. Ultraviolet photoelectron spectroscopy (UPS) measurements were performed using an Omicron Nanotechnology ESCA+S instrument with helium discharge lamp (He I line, 21.2 eV) as the UV excitation source and a hemispherical SPHERA energy analyzer at a base pressure of 4×10^{-10} mbar. For these measurements, 10−20 nm thick films were spin-coated onto ITO/PEDOT:PSS substrates inside a glovebox (nitrogen, <1 ppm of O_2, <1 ppm of H_2O), and transferred into the UPS chamber with <30 s of air exposure. All UPS measurements were carried out at a −3 V sample bias to collect the low kinetic energy electrons.

Device Performance Characterization. Device power conversion efficiency (PCE) measurements were carried out inside a glovebox under nitrogen atmosphere unless otherwise stated. Current density−voltage (J−V) characteristics were measured using a Keithley 2400 sourcemeter unit. An AM 1.5 G solar simulator (Newport 91160) with an intensity of 100 mW/cm^2 was used as a light source, and was calibrated using silicon reference cells with KG5 filter. Absorption spectra of device films were obtained using a Shimadzu Corporation UV-3600 UV−VIS−NIR spectrophotometer. External quantum efficiency (EQE) measurements were obtained on encapsulated devices in air using a Newport system.

Morphological Analyses. Active-layer morphology characterizations by grazing incidence wide-angle X-ray diffraction (GIXD) experiments carried out at Beamline 7.3.3 of the Advanced Light Source (ALS) at Lawrence Berkeley National Lab (LBNL). Samples of Sq-TAA-OH, $PC_{71}BM$, and 1:5 Sq-TAA-OH:$PC_{71}BM$ blend were spin-coated onto substrates having a PEDOT:PSS layer fabricated on a silicon wafer, using the same film preparation procedures used to make the corresponding OPV devices. An X-ray beam impinged onto the sample at a grazing angle slightly above the critical angle of the polymer film (R_c = 0.16°) but below the critical angle of the Si substrate (R_c = 0.28°). The wavelength of the X-rays was 1.240 Å. The scattered intensity was recorded using a Pilatus 1 M detector with image sizes of 981 × 1043 pixels, where each pixel was 0.172 × 0.172 mm^2.

Crystallography. Room-temperature X-ray diffraction measurements were carried out using a Bruker-Nonius KappaCCD instrument having a MoKα source with λ = 0.71073 Å radiation, using a single crystal of Sq-TAA-OH grown from acetone overlayered with hexane. Structures were solved by direct methods based on F^2 through a full-matrix least-squares routine using the program SHELXL.[43,44] All heavy atom positions where directly identified, and hydrogen atom positions set using a standard riding model. Further details are given in the Supporting Information in CIF file format.

ASSOCIATED CONTENT

Supporting Information

Additional photovoltaic device characterization data, GIWAXS diffractogram for Sq-TAA-OH spin-coated film, crystallographic data collection, and structural data for Sq-TAA-OH. CCDC 988940 reports supplementary crystallographic data for this article. This material is available free of charge via the Internet at http://pubs.acs.org/.

AUTHOR INFORMATION

Corresponding Authors

*E-mail: lahti@chem.umass.edu.
*E-mail: thai@chem.umass.edu.

Notes

The authors declare no competing financial interest.

ACKNOWLEDGMENTS

This work was supported as part of Polymer-Based Materials for Harvesting Solar Energy, an Energy Frontier Research Center funded by the U.S. Department of Energy, Office of Science, Basic Energy Sciences, under Award DE-SC0001087. Morphological studies were performed at beamlines 11.0.1.2 and 7.3.3 at the Advanced Light Source, Lawrence Berkeley National Laboratory, which is supported by the Department of Energy, Office of Science, Office of Basic Energy Sciences, under Contract DE-AC02-05CH11231.

REFERENCES

(1) Li, H.; Giri, G.; Tok, J. B. H.; Bao, Z. Toward High-Mobility Organic Field-Effect Transistors: Control of Molecular Packing and Large-Area Fabrication of Single-Crystal-Based Devices. *MRS Bull.* **2013**, *38*, 34−42.

(2) Sasabe, H.; Kido, J. Recent Progress in Phosphorescent Organic Light-Emitting Devices. *Eur. J. Chem.* **2013**, *34*, 7653−7663.

(3) Sasabe, H.; Kido, J. Development of High Performance OLEDs for General Lighting. *J. Mater. Chem. C* **2013**, *1*, 1699−1707.

(4) Dou, L.; You, J.; Hong, Z.; Xu, Z.; Li, G.; Street, R. A.; Yang, Y. 25th Anniversary Article: A Decade of Organic/Polymeric Photovoltaic Research. *Adv. Mater.* **2013**, *25*, 6642−6671.

(5) Janssen, R. A. J.; Nelson, J. Factors Limiting Device Efficiency in Organic Photovoltaics. *Adv. Mater.* **2013**, *25*, 1847−1858.

(6) Grätzel, M. Recent Advances in Sensitized Mesoscopic Solar Cells. *Acc. Chem. Res.* **2009**, *42*, 1788−98.

(7) Osedach, T. P.; Andrews, T. L.; Bulović, V. Effect of Synthetic Accessibility on the Commercial Viability of Organic Photovoltaics. *Energy Environ. Sci.* **2013**, *6*, 711−718.

(8) Darling, S. B.; You, F. Q. The Case for Organic Photovoltaics. *RSC Adv.* **2013**, *3*, 17633−17648.

(9) Yue, D.; Khatav, P.; You, F.; Darling, S. B. Deciphering the Uncertainties in Life Cycle Energy and Environmental Analysis of Organic Photovoltaics. *Energy Environ. Sci.* **2012**, *5*, 9163−9172.

(10) Peumans, P.; Yakimov, A.; Forrest, S. R. Small Molecular Weight Organic Thin-Film Photodetectors and Solar Cells. *J. Appl. Phys.* **2003**, *93*, 3693−3723.

(11) Jo, J.; Na, S.; Kim, S.; Lee, T.; Chung, Y.; Kang, S.; Vak, D.; Kim, D. Three-Dimensional Bulk Heterojunction Morphology for Achieving High Internal Quantum Efficiency in Polymer Solar Cells. *Adv. Funct. Mater.* **2009**, *19*, 2398−2406.

(12) Ma, W.; Yang, C.; Gong, X.; Lee, K.; Heeger, A. J. Thermally Stable, Efficient Polymer Solar Cells with Nanoscale Control of the Interpenetrating Network Morphology. *Adv. Funct. Mater.* **2005**, *15*, 1617−1622.

(13) Yang, X.; Loos, J.; Veenstra, S. C.; Vehees, W. J. H.; Wienk, M. M.; Michels, M. A. J.; Janssen, R. A. J. Nanoscale Morphology of High-Performance Polymer Solar Cells. *Nano Lett.* **2005**, *5*, 579−583.

(14) Li, G.; Shrotriya, V.; Huang, J. S.; Yao, Y.; Moriarty, T.; Emery, K.; Yang, Y. High-Efficiency Solution Processable Polymer Photovoltaic Cells by Self-Organization of Polymer Blends. *Nat. Mater.* **2005**, *4*, 864−868.

(15) Lee, J. K.; Ma, W. L.; Brabec, C. J.; Yuen, J.; Moon, J. S.; Kim, J. Y.; Lee, K.; Bazan, G. C.; Heeger, A. J. Processing Additives for Improved Efficiency from Bulk Heterojunction Solar Cells. *J. Am. Chem. Soc.* **2008**, *130*, 3619−3623.

(16) Moulé, A. J.; Meerholz, K. Controlling Morphology in Polymer−Fullerene Mixtures. *Adv. Mater.* **2008**, *20*, 240−245.

(17) Peet, J.; Kim, J. Y.; Coates, N. E.; Ma, W. L.; Moses, D.; Heeger, A. J.; Bazan, G. C. Efficiency Enhancement in Low-Bandgap Polymer Solar Cells by Processing with Alkane Dithiols. *Nat. Mater.* **2007**, *6*, 497−500.

(18) Liao, H.-C.; Ho, C.-C.; Chang, C.-Y.; Jao, M.-H.; Darling, S. B.; Su, W-F. Additives for morphology control in high-efficiency organic solar cells. *Mater. Today* **2013**, *16*, 326−336.

(19) Yang, F.; Shtein, M.; Forrest, S. R. Controlled growth of a molecular bulk heterojunction photovoltaic cell. *Nat. Mater.* **2005**, *4*, 37−41.

(20) Sun, S.; Fan, Z.; Wang, Y.; Haliburton, J. Organic solar cell optimizations. *J. Mater. Sci.* **2005**, *40*, 1429−1443.

(21) Hu, L.; Yan, Z.; Xu, H. Advances in synthesis and application of near-infrared absorbing squaraine dyes. *RSC Adv.* **2013**, *3*, 7667−7676.

(22) Wei, G.; Wang, S.; Renshaw, K.; Thompson, M. E.; Forrest, S. R. Solution-Processed Squaraine Bulk Heterojunction Photovoltaic Cells. *ACS Nano* **2010**, *4*, 1927−1934.

(23) Chen, G.; Sasabe, H.; Wang, Z. Q.; Wang, X. F.; Hong, Z. R.; Yang, Y.; Kido, J. Co-Evaporated Bulk Heterojunction Solar Cells with >6.0% Efficiency. *Adv. Mater.* **2012**, *24*, 2768−2773.

(24) Chen, G.; Yokoyama, D.; Sasabe, H.; Hong, Z. R.; Yang, Y.; Kido, J. Optical and electrical properties of a squaraine dye in photovoltaic cells. *Appl. Phys. Lett.* **2012**, *101*, 083904/1−4.

(25) Silvestri, F.; Irwin, M. D.; Beverina, L.; Facchetti, A.; Pagani, G. A.; Marks, T. J. Efficient Squaraine-Based Solution Processable Bulk-Heterojunction Solar Cells. *J. Am. Chem. Soc.* **2008**, *130*, 17640−17641.

(26) Wang, S. Y.; Mayo, E. I.; Perez, M. D.; Griffe, L.; Wei, G. D.; Djurovich, P. I.; Forrest, S. R.; Thompson, M. E. High efficiency

organic photovoltaic cells based on a vapor deposited squaraine donor. *Appl. Phys. Lett.* **2009**, *94*, 233304/1−3.

(27) Wei, G. D.; Wang, S. Y.; Renshaw, K.; Thompson, M. E.; Forrest, S. R. Solvent-Annealed Crystalline Squaraine: $PC_{70}BM$ (1:6) Solar Cells. *ACS Nano* **2010**, *4*, 1927−1934.

(28) Wei, G. D.; Wang, S. Y.; Sun, K.; Thompson, M. E.; Forrest, S. R. *Adv. Energy Mater.* **2011**, *1*, 184−187.

(29) Song, B.; Rolin, C.; Zimmerman, J. D.; Forrest, S. R. Effect of Mixed Layer Crystallinity on the Performance of Mixed Heterojunction Organic Photovoltaic Cells. *Adv. Mater.* **2014**, *26*, 2914−2918.

(30) Chen, G.; Sasabe, H.; Wang, Z.; Wang, X.; Hong, Z.; Kido, J.; Yang, Y. Solution-processed organic photovoltaic cells based on a squaraine dye. *Phys. Chem. Chem. Phys.* **2012**, *14*, 14661−14666.

(31) Della Pelle, A. M.; Homnick, P. J.; Bae, Y.; Lahti, P. M.; Thayumanavan, S. Effect of Substituents on Optical Properties and Charge-Carrier Polarity of Squaraine Dyes. *J. Phys. Chem. C* **2014**, *118*, 1793−1799.

(32) Wang, S.; Hall, L.; Diev, V. V.; Haiges, R.; Wei, G.; Xiao, X.; Djurovich, P. I.; Forrest, S. R.; Thompson, M. E. *N,N*-Diarylanilinosquaraines and Their Application to Organic Photovoltaics. *Chem. Mater.* **2011**, *23*, 4789−4798.

(33) Qi, B.; Wang, J. Fill Factor in Organic Solar Cells. *Phys. Chem. Chem. Phys.* **2013**, *15*, 8972−8982.

(34) Staniec, A.; Parnell, A. J.; Dunbar, A. D. F.; Yi, H.; Pearson, A. J.; Wang, T.; Hopkinson, P. E.; Kinane, C.; Dalgliesh, R. M.; Donald, A. M.; Ryan, A. J.; Iraqi, A.; Jones, R. A. L.; Lidzey, D. G. The Nanoscale Morphology of a PCDTBT:PCBM Photovoltaic Blend. *Adv. Energy Mater.* **2011**, *1*, 499−504.

(35) Wei, G.; Lunt, R. R.; Sun, K.; Wang, S.; Thompson, M. E.; Forrest, S. R. Efficient, Ordered Bulk Heterojunction Nanocrystalline Solar Cells by Annealing of Ultrathin Squaraine Thin Films. *Nano Lett.* **2010**, *10*, 3555−3559.

(36) Wei, G.; Xiao, X.; Wang, S.; Sun, K.; Bergemann, K. J.; Thompson, M. E.; Forrest, S. R. Functionalized Squaraine Donors for Nanocrystalline Organic Photovoltaic. *ACS Nano* **2012**, *6*, 972−978.

(37) Dirk, C. W.; Herndon, W. C.; Cervantes-Lee, F.; Selnau, H.; Martinez, S.; Kalamegham, P.; Tan, A.; Campos, G.; Velez, M.; Zyss, J.; Ledoux, I.; Cheng, L.-T. Squarylium Dyes: Structural Factors Pertaining to the Negative Third-Order Nonlinear Optical Response. *J. Am. Chem. Soc.* **1995**, *117*, 2214−2225.

(38) Liu, F.; Gu, Y.; Jung, J. W.; Jo, W. H.; Russell, T. P. On the morphology of polymer-based photovoltaics. *J. Polym. Sci., Part B: Polym. Phys.* **2012**, *50*, 1018−1044.

(39) Liu, F.; Gu, Y.; Shen, X.; Ferdous, S.; Wang, H.-W.; Russell, T. P. Characterization of the Morphology of Solution-Processed Bulk Heterojunction Organic Photovoltaics. *Prog. Polym. Sci.* **2013**, *38*, 1990−2052.

(40) Guo, C.; Kozub, D. R.; Vajjala Kesava, S.; Wang, C.; Hexemer, A.; Gomez, E. D. Signatures of Multiphase Formation in the Active Layer of Organic Solar Cells from Resonant Soft X-ray Scattering. *ACS Macro Lett.* **2013**, *2*, 185−189.

(41) Chen, W.; Nikiforov, M. P.; Darling, S. B. Morphology characterization in organic and hybrid solar cells. *Energy Environ. Sci.* **2012**, *5*, 8045−8074.

(42) Liu, F.; Wang, C.; Baral, J. K.; Zhang, L.; Watkins, J. J.; Briseño, A.; Russell, T. P. Relating Chemical Structure to Device Performance via Morphology Control in Diketopyrrolopyrrole-Based Low Band Gap Polymers. *J. Am. Chem. Soc.* **2013**, *135*, 19248−19259.

(43) Sheldrick, G. M. A Short History of SHELX. *Acta Crystallogr., Sect A* **2008**, *64*, 112−122.

(44) Sheldrick, G. M. *SHELXTL97, Program for the Refinement of Crystal Structures*; University of Göttingen: Göttingen, Germany.